CrossMark

TECHNICAL ARTICLE

High-temperature Deformation Behavior of HP40Nb Micro-alloyed Reformer Steel

Amitava Ghatak[1] · P. S. Robi[1]

Abstract Reformer tubes are designed for prolonged service conditions at high temperatures and pressures in petrochemical industries for the production of hydrogen-rich gas. Frequent premature failures of reformer tubes are encountered due to the microstructural degradation of the material. Analysis of the tensile and creep deformation behavior of HP40Nb micro-alloyed steel at temperatures ranging from 800 to 1200 °C is presented in this paper. The Young's modulus, yield strength, and ultimate tensile strength of the micro-alloyed steel decreased, and the ductility increased with the increase in temperature up to 1000 °C. The stress–temperature-dependent steady state creep rate obeys Young's modulus compensated power-law relationship. The stress exponent and activation energy for creep were determined to be 7.96 and 332.65 kJ/mol. The predicted minimum creep rates were compared with the experimental values. It is possible to predict the value of minimum creep rate within an error less than ±7%. Analysis of fractured surfaces reveals brittle fracture up to 800 °C, while at higher temperature, dimple fractures are predominant.

✉ Amitava Ghatak
a.ghatak@iitg.ernet.in

1 Department of Mechanical Engineering, Indian Institute of Technology Guwahati, Guwahati, India

Introduction

Last few decades has witnessed increasing energy demand with simultaneous ever increasing cost of oil and its bi-products across the world. In-house production of gases such as ammonia, methane, ethane, synthesis gas, and hydrogen are commonly manufactured in fertilizer and petrochemical industries. Hydrogen gas is generally produced by catalytic reaction of hydro-carbons and steam at temperatures in the range 750–1000 °C and gas pressure around 2.3–2.8 MPa inside reformer tubes. These reformer tubes are designed to withstand the gas pressures and high service temperature for extended period of time. Austenitic stainless steels which can withstand higher temperature and stress for prolonged time have been used as the material of reformer furnace tubes for the last 6–7 decades. The development of material for the reformer tubes has undergone several modifications, and presently, the material which is extensively used is the centrifugally cast HP40Nb micro-alloyed stainless steel which exhibits high creep and corrosion resistance. Although these micro-alloyed steel tubes are designed to withstand the severe service conditions, incidents like premature failure of the tubes due to creep are frequent. The high nickel concentration (Ni 35 wt%) along with 25 wt% Cr and 1.6 wt% Si in HP40Nb steel results in austenitic structure, which is a main requirement in the development of creep resistant materials. The structure of this micro-alloyed steel consists of primary austenite dendrites and various carbides at the grain boundary regions. The presence of carbides at the grain boundaries contribute to the high creep resistance of the material [1].

Investigations regarding microstructure and mechanical properties of HP40Nb steel, mainly the effect of aluminum [2], tungsten [1, 3], titanium [1], and overheating temperature [4], have been reported by researchers. The creep life of reformer steel tubes has also been predicted by parametric

techniques [5–9]. Though in most of the cases, the remaining creep life of service exposed HP40Nb micro-alloyed steel tubes were estimated by Larson–Miller parameter [6, 10]. The creep deformation behavior of this micro-alloyed steel has not been investigated.

Attempts were made to explain the creep deformation behavior of metallic materials by various models. Among the various models, it appears that the creep deformation behavior HP40Nb micro-alloyed steel can be modeled based on the modulus compensated power-law equation proposed by Barrett et al. [11]. By this model, the stress–temperature dependence of minimum creep rate can be expressed by the relationship [11–13]:

$$\dot{\varepsilon} = A \left(\frac{\sigma}{E(T)} \right)^n \exp \left(-\frac{Q}{RT} \right), \tag{1}$$

where $\dot{\varepsilon}$ is the minimum creep rate, σ is the applied stress, E is the Young's modulus of the steel, R the universal gas constant, T the absolute temperature, Q the activation energy for creep, and A and n are constants.

In the present study, the microstructure and tensile properties of HP40Nb micro-alloyed steel at elevated temperatures were investigated. Creep experiments were carried out at various temperatures and stresses, and the creep deformation behavior of the material is explained based on the Young's modulus compensated power-law relationship.

Experimental Procedures

The material used for the present study was centrifugally cast HP40Nb reformer steel tube. The material was cut from the extreme top portion of a 15-m-long vertically placed reformer tube where the section was exposed to 650 °C. Since this reformer tube was designed to operate at 995 °C for 11½ years, it is expected that the exposure of the investigated section of the tube at 650 °C may not lead to any microstructural degradation. The outer diameter and thickness of the reformer tube were 136 and 15.3 mm, respectively. Table 1 shows the chemical composition of the micro-alloyed steel, which was analyzed by optical emission spectrometer.

Specimens for the microstructural investigation were prepared following the standard metallographic procedure. The specimens were cut from the as-received reformer tube by wire-cut electrical discharge machining (EDM) and

Table 1 Chemical composition of the steel (wt%)

C	Cr	Ni	Si	Nb	Ti	Mo	Fe
0.4	23.6	34.9	1.3	0.8	0.037	0.037	Balance

mounted in thermoplastic resin using a hot mounting press. Specimens polished using a series of abrasive papers followed by final polishing using 0.5-μm-sized diamond paste. The specimens were subsequently etched using Glyceregia etchant (15 ml HCl + 10 ml Glycerol + 5 ml HNO_3). Microstructural characterizations were carried out using optical microscopy (OM) and scanning electron microscopy (SEM). The chemical compositions of various phases present in the matrix were analyzed using an energy dispersive x-ray spectroscope (EDS) attached to the SEM. The grain size was determined by line intercept method. The second-phase particles present in the as-received micro-alloyed steel matrix were identified by x-ray diffraction (XRD) technique. The XRD was carried out at a tube voltage of 50 kV and 180 mA using Cu-Kα radiation ($\lambda = 1.5405$ Å), and the pattern was recorded over a 2θ range of 30° to 80°. The peak position and intensity of the XRD pattern was compared with JCPDS datasheet to identify the phases present in the as-received micro-alloyed steel.

Hardness distribution across the thickness of tube wall was measured using Vickers hardness tester with 30 kg load. Dog-bone-shaped flat tensile specimens having cross sectional area of 6.5 mm × 3 mm and gauge length 25 mm were machined using wire-cut EDM. Axis of the machined tensile specimens was kept parallel to the longitudinal axis of the reformer tube. Room temperature and elevated temperature tensile tests were carried out using a 100 kN capacity servo hydraulic controlled universal testing machine (UTM) equipped with a 2-zone resistance heated split furnace. Tensile tests were carried out at constant temperatures maintained within an accuracy of ±1 °C. The specimen was loaded till failure at a constant cross-head speed of 0.05 mm/min. During the tensile test, the specimen gauge length extension was measured using a high-temperature extensometer. Tensile test was performed at room temperature, 600, 800, 1000, and 1200 °C. From the tensile test data, the Young's modulus E, yield strength YS (0.2% proof stress), ultimate tensile strength UTS, and total strain to failure were determined.

Tensile creep experiments were carried out at constant stresses 47, 68, and 80 MPa at 800, 850, and 900 °C. The experiments were performed using an in-house-developed constant stress creep testing set-up. The specimens were heated using an impedance heating system, and the temperature during the tests was controlled with an accuracy of ±3 °C. During creep tests, the gauge length extensions of creep specimen were recorded using a professional high-definition video camera. The picture frames of the digital video recording at regular time intervals during creep deformation were extracted, and the respective gauge length elongation was determined by image analysis technique to obtain the creep strain. Minimum creep rate $\dot{\varepsilon}$ of

each creep curve was determined by differentiating the creep curve which was used for further analysis. The constitutive parameters of Eq. 1 were determined by the least squares technique by minimizing the error between the predicted and experimentally obtained values of $\dot{\varepsilon}$.

Results and Discussion

Figure 1(a) and (b) shows OM of the as-received reformer tube taken at two different magnifications. Low-magnification micrograph shown in Fig. 1(a) reveals dendritic structure. A network of second-phase particles is observed at the inter-dendritic regions. Microstructure (Fig. 1a) reveals equiaxed grains with a continuous network of carbides at grain boundary regions. Based on light contrast, high-magnification observation (Fig. 1b) reveals two types of second-phase particles at the grain boundary regions. One is a light-colored phase having laminar type (or skeleton form) features, whereas the other is dark colored having fine particle like features.

Figure 2 shows the SEM micrograph of the as-received micro-alloyed steel specimen. Backscattered electron (BSE) images observed under SEM reveal three different particles at the grain boundary regions of the austenitic matrix: (i) a dark gray phase (phase-A) having a laminar (or skeleton type feature) type morphology, which was the major constituent of the second-phase particles at the grain boundary region, (ii) a white phase (phase-B) segregated at grain boundary, and (iii) small quantities of very fine phase white particles (phase-C). Since the BSE electron image contrasts are based on the atomic number of elements, the higher intensity or white regions are associated with a higher atomic number element. From the EDS spectrum shown in Fig. 3, phase-A, phase-B, and phase-C are identified as Cr-rich carbide, Nb-rich carbide, and (Nb,Ti)-rich carbide, respectively.

Figure 4(a) shows the distribution of Fe, Cr, Nb, Ti, and Si obtained by x-ray elemental mapping. The large second-phase particle is identified as chromium carbide, whereas the small precipitate on the micrograph is Nb-rich carbide. The less amount of Ti is also present with the Nb-rich carbide. The elemental mapping of the as-received micro-alloyed steel confirms the results obtained by the EDS. Figure 4(b) shows the XRD pattern of the as-received micro-alloyed steel sample. A comparison of the peaks with the JCPDS data indicates the presence of gamma (γ), Cr_7C_3, NbC, TiC, and $Cr_{23}C_6$. The crystal structure of these phases are FCC ($a = 3.6$ Å), orthorhombic ($a = 7.014$ Å, $b = 12.15$ Å, $c = 4.532$ Å), FCC ($a = 10.65$ Å), FCC ($a = 4.4$ Å), and FCC ($a = 4.6$ Å), respectively.

Figure 5 shows the variation of the grain size and Vickers hardness of the micro-alloyed steel across the wall thickness of reformer tube. The figure shows a marginal increase in grain size from 67 μm at the inside surface to 73 μm at the outside surface of the tube. Almeida et al. [14] and Alvino et al. [7] reported coarse grains at the outer surface compared to the inside surface of the centrifugally cast HP40Nb steel. In addition, no evidence of any type of defect like sub-micron sized voids at austenite grains, grain
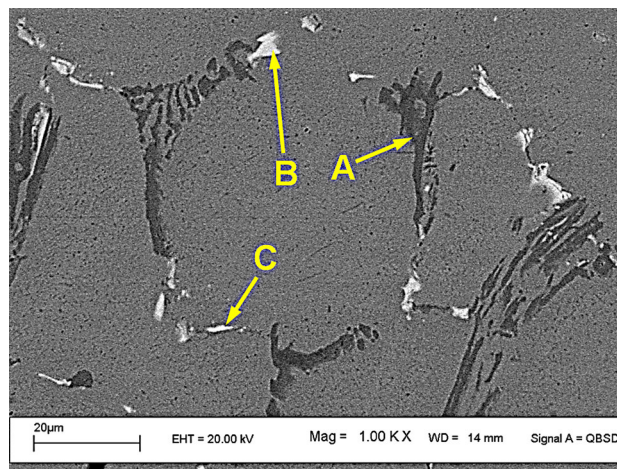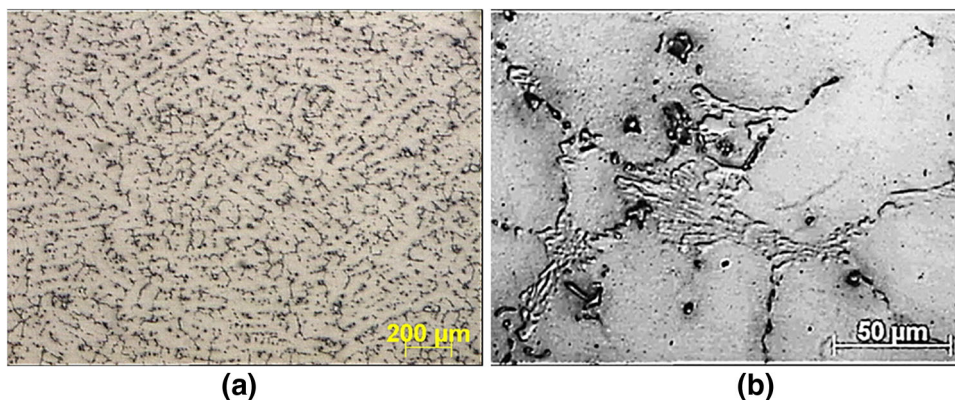

Fig. 2 SEM backscattered electron image of the as-received steel with phase-A, phase-B, and phase-C in matrix

Fig. 1 Optical micrographs of the steel at (**a**) low magnification and (**b**) high magnification
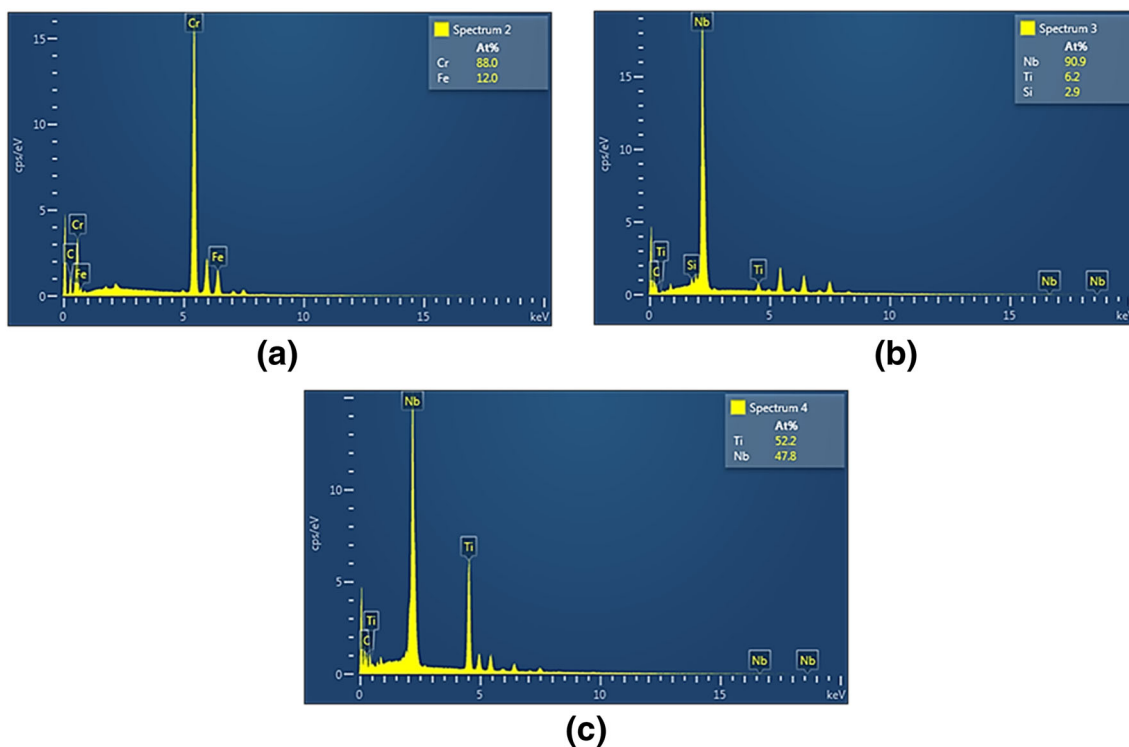

(a) (b)

Fig. 3 EDS spectrum of the (**a**) phase-A, (**b**) phase-B, and (**c**) phase-C in the as-received steel

boundaries, or particle–matrix interface was observed under SEM even at higher magnifications of 10,000 X. In Fig. 5, only a marginal (∼4.5%) increase in the hardness is observed across the tube thickness of reformer tube. The hardness value is higher than that reported in literature by various authors [15]. This difference is due to the fact that the literature reported values are for the steels that have failed during service by creep deformation. From the above results, it can be inferred that the material has not undergone any microstructural degradation due to the service exposure at 650 °C prior to the present study.

Tensile properties of the micro-alloyed steel were determined from the tensile data. The plots of Young's modulus and total strain to failure versus temperature are shown in Fig. 6(a) and (b), respectively. The E value decreases marginally with the increase in temperature up to 600 °C. E value decreases rapidly from 165 GPa at 600 °C to 38 GPa at 1200 °C. As can be seen in Fig. 6a, the variation of E with temperature is expressed by a second-order polynomial function in the form:

$$E(T) = -0.0002T^2 + 0.1917T + 126. \quad (2)$$

The coefficient of determination R^2 for this expression is 0.98, indicating a very good fit.

From Fig. 6(b), it is evident that the total strain to failure increases with increase in temperature and attains a maximum value at 1000 °C. The ductility decreases with further increase in test temperature. As the test temperature is increased from 1000 to 1200 °C, the total strain to failure decreases from 0.204 to 0.075. As shown in Table 2, the YS and UTS decrease continuously with the increase in temperature.

The specimen tested at lower temperatures revealed flat fracture, indicating the brittle nature of the material. Necking was observed in the sample tested at 800 and 1000 °C, indicting ductile mode of failure. Figure 7(a)–(h) shows the SEM fractographs of the specimen tensile tested at room temperature and elevated temperatures. Low-magnification observation (Fig. 7a) of the fractured surface of the specimen tested at room temperature reveals quasi-cleavage features. The figure shows a number of large voids like features on the fracture surface. Observation at high magnification, as shown in Fig. 7(b), reveals trans-granular cleavage features and micro-cracks on the fracture surface, indicating the dominant failure mechanism as a brittle fracture. Figure 7(c)–(f) shows the fractographs of tensile tested specimens at 800 and 1000 °C. The features indicate extensive plastic deformation of the grains before final failure. Since the microstructure of the material revealed the presence of carbides at grain boundary regions, during the tensile loading at temperatures up to 1000 °C, the main mechanism of failure can be considered as due to deformation of the grains by multiple slip rather than by micro-void coalescence. The

Fig. 4 (**a**) Elemental mapping and (**b**) XRD pattern of the as-received steel

(a)

(b)
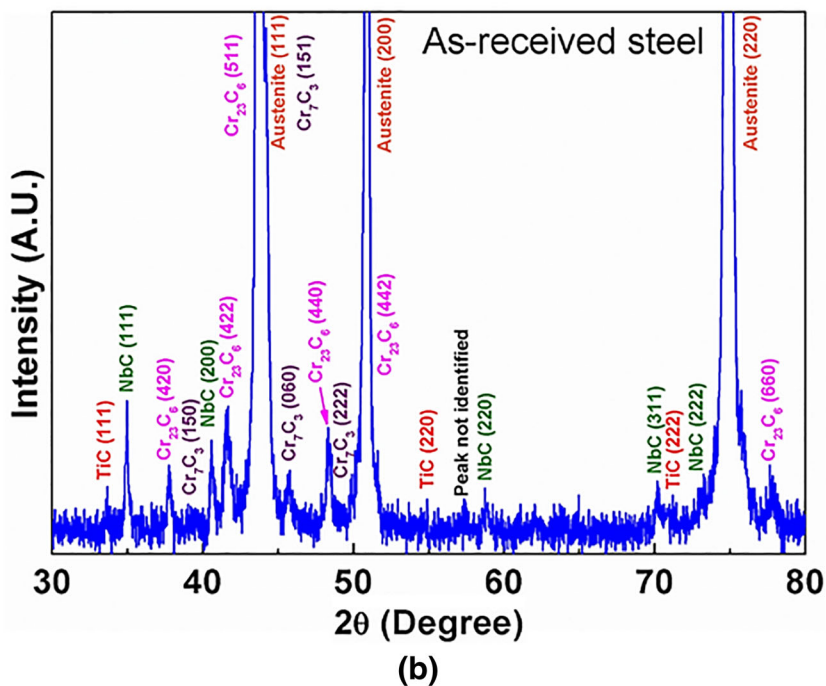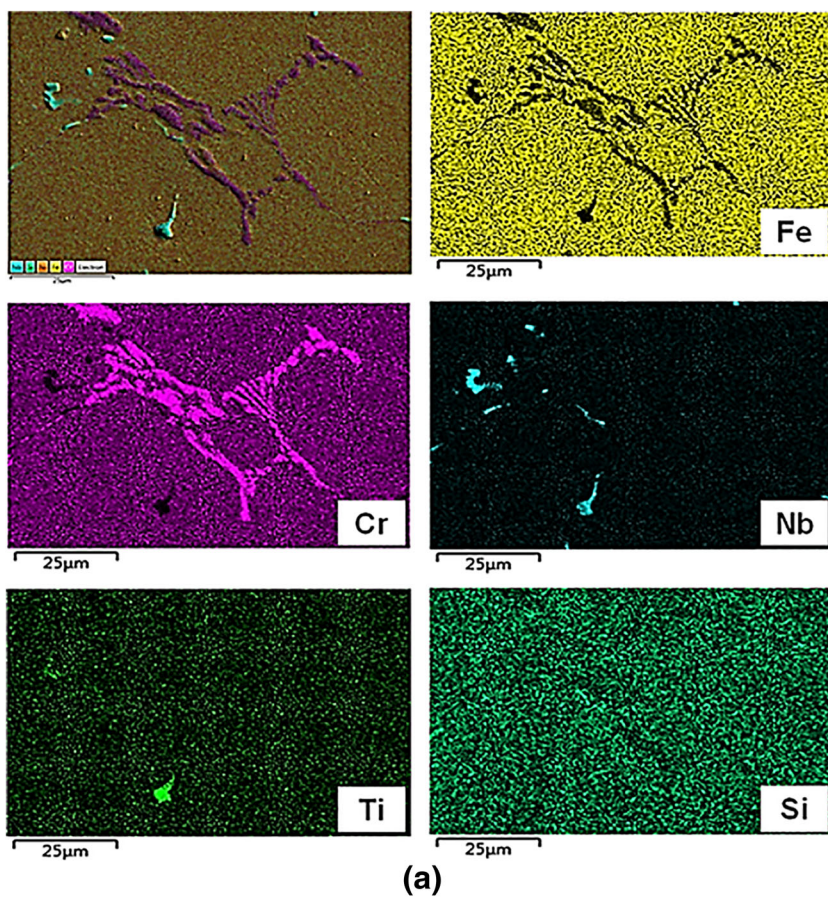
fractographs shown in Fig. 7(g) and (h) indicate inter-granular failure in the material when tested at 1200 °C. Low-magnification observation indicates the presence of large voids, whereas at high magnification, fractograph shows voids and micro-cracks at particle–matrix interface and grain boundary regions.

Figure 8(a) shows the strain versus time plot obtained during the accelerated creep test carried out at 800 °C and 47 MPa. The creep curve shows the primary, secondary, and tertiary creep region. The secondary creep region is characterized by a constant creep rate. Toward the end of the secondary creep region, the strain rate increases, indicating degradation in microstructure, and it enters the region of tertiary creep, resulting in the final failure of the specimen. It may be noted that the strain in the tertiary creep regime is almost 25% of the total creep strain, indicating that the secondary creep region is the major contributor to the total creep strain. Figure 8(b) shows the plot of strain rate versus creep strain, illustrating the three distinct creep regimes. During primary creep, creep rate decreases rapidly and approaches a minimum value at secondary creep regime. The creep rate accelerates in the tertiary creep region, resulting in the final failure.

A double logarithmic plot of minimum creep rate versus Young's modulus compensated applied stress at constant temperatures is illustrated in Fig. 9. For obtaining this plot,
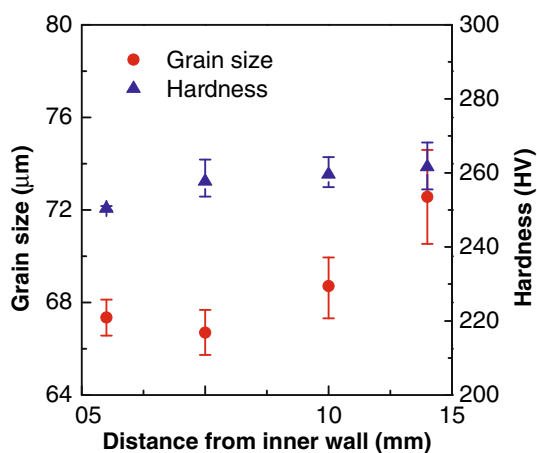
the E value was determined using Eq. 2. The figure indicates that the minimum creep rate increases with increase in σ/E and decrease in temperature.

For the development of the constitutive equation for creep deformation, the values of the parameters, viz. constant A, stress exponent n, and activation energy for creep Q of Eq. 1, were determined by the least squares method. In the least squares fit method, the functional error between the experimental and predicted minimum creep rate was minimized. The optimized values of three constitutive parameters, A, n, and Q of Eq. 1 are found to be 2.87×10^{36} s^{-1}, 7.96, and 332.65 kJ/mol.

In pure metals, depending on the value of n, the creep deformation mechanism during the secondary stage can be either by diffusion creep ($n = 1$), grain boundary sliding ($n = 2$), and dislocation creep ($n \geq 3$) mechanisms. Latha et al. [16] and Park et al. [17] reported the value of n in the range 3–12 for the austenitic stainless steels. Figure 10 shows the plot of temperature-compensated creep rate ($C\dot{\varepsilon}\exp(Q/RT)$) versus normalized stress (σ/E) of the experimental creep data, where the value of C is equal to $1/A$. From the slope of the curve, the value of n is determined as 7.69 with an R^2 value of 0.96. The value of $n = 7.96$ indicates that the secondary stage creep deformation is controlled by dislocation creep mechanism. The activation energy for vacancy self-diffusion (Q_c) in austenite is 270 kJ/mol [17]. The activation energy for creep (332.65 kJ/mol) obtained in the present study is higher than

Fig. 5 Variation of hardness and grain size across the wall thickness of the reformer tube

Table 2 Tensile test results at elevated temperatures

Temperature (°C)	YS (MPa)	UTS (MPa)	Strain to failure
27	213	365	0.06324
600	130	331	0.10813
800	86	119	0.16342
1000	32	43	0.20353
1200	20	21	0.07515

Fig. 6 Variation of (**a**) Young's modulus and (**b**) total strain to failure with temperature
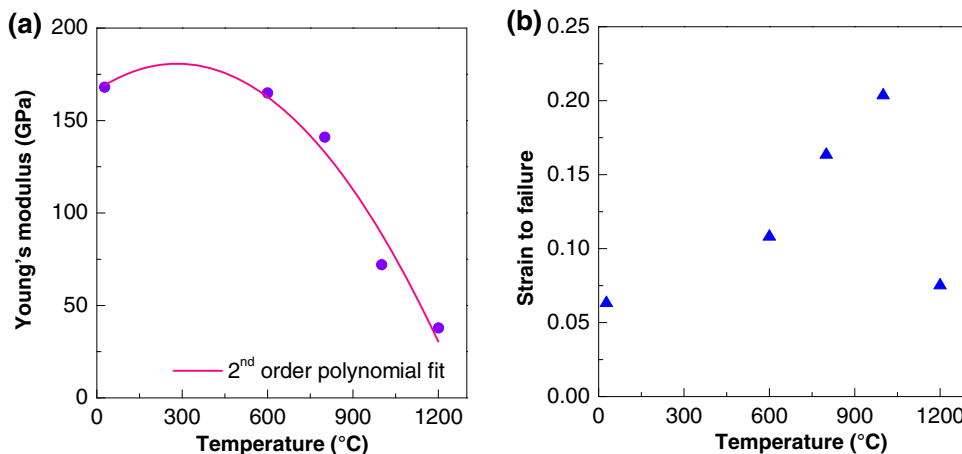
Fig. 7 SEM fractographs of tensile tested specimens at (**a**) and (**b**) room temperature, (**c**) and (**d**) 800 °C, (**e**) and (**f**) 1000 °C, and (**g**) and (**h**) 1200 °C at lower and higher magnifications
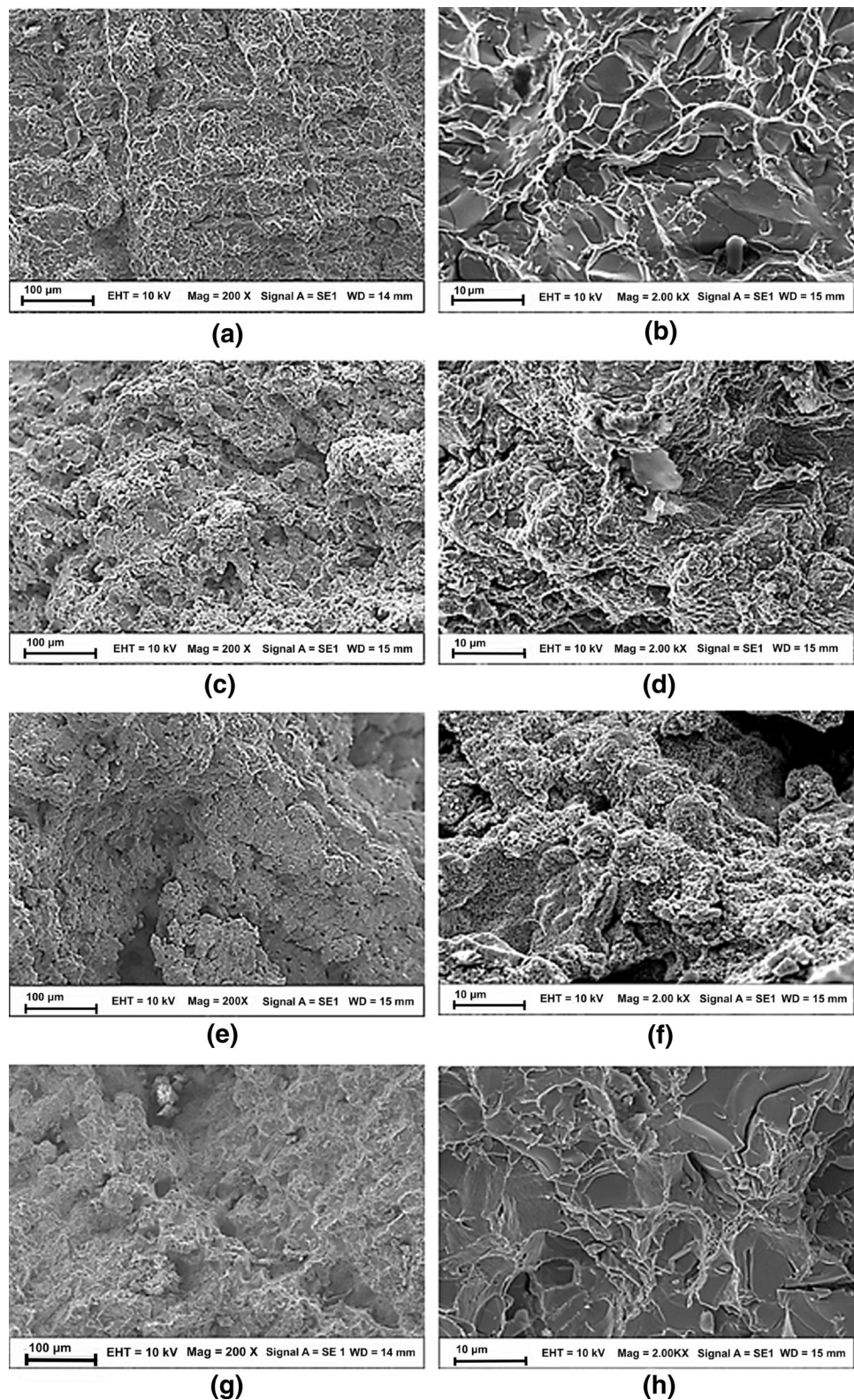
the Q_c. The higher activation energy in the present case is due to the presence of carbides which act as barriers in the slip plane for the dislocation movement. Further movement of dislocations is favored by dislocation climb across adjacent slip planes and hence higher activation energy for creep. Higher activation energy for creep in different

Fig. 8 Plot of (a) creep curve
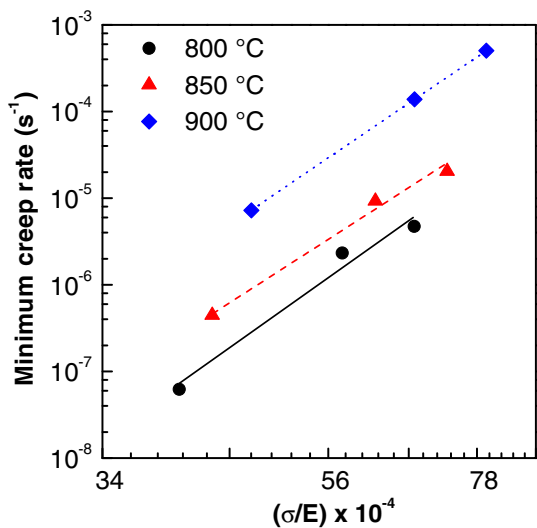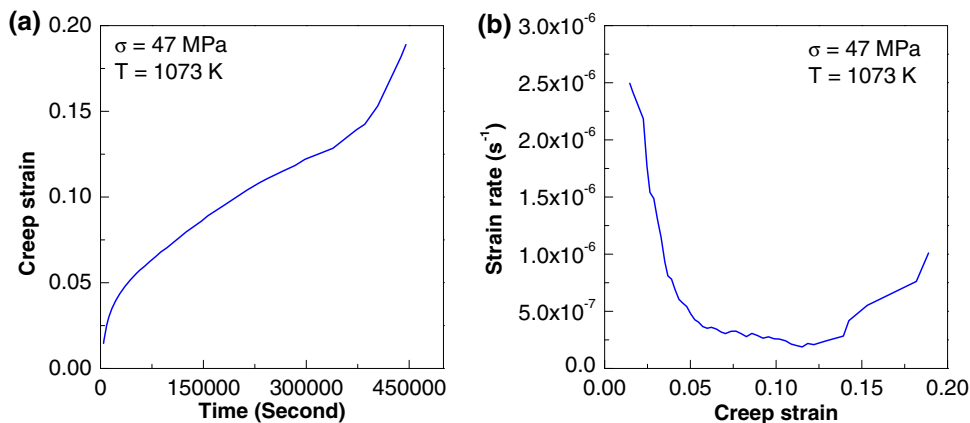and (b) creep rate versus creep
strain at 800 °C/47 MPa

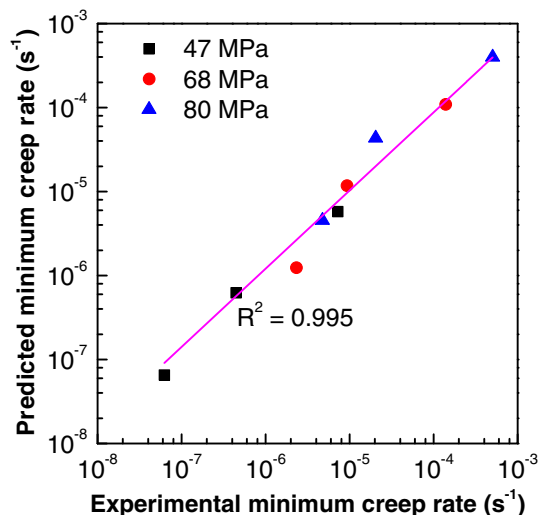Fig. 9 Minimum creep rate versus σ/E at constant temperatures

Fig. 10 Temperature-compensated minimum creep rate versus normalized stress

Fig. 11 Variation of predicted minimum creep rate with experimental minimum creep rate using power-law

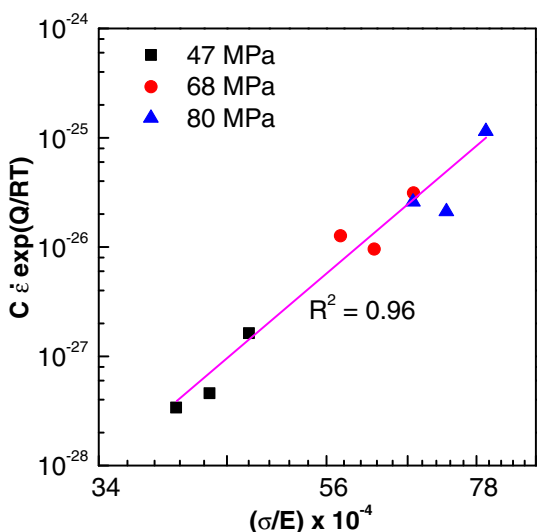stainless steels has also been reported by various researchers [17–22].

The constitutive equation for the creep deformation, arrived by substituting the values of A, n, Q and $E(T)$ in Eq. 1, is expressed as

$$\dot{\varepsilon} = 2.87 \times 10^{36} \left(\frac{\sigma}{-0.0002T^2 + 0.1917T + 126} \right)^{7.96} \times \exp\left(-\frac{332652}{RT} \right). \tag{3}$$

Figure 11 shows the plot of experimental values of minimum creep rate and the minimum creep rate predicted by Eq. 3 for the micro-alloyed steel. All points in the figure lie very close to the line inclined at 45°, indicating good prediction of minimum creep rate. The R^2 between the experimental values of minimum creep rate and predicted minimum creep rate is found to be 0.995. It is observed that the percentage error in the prediction of $\ln(\dot{\varepsilon})$ for the

Fig. 12 (**a**) Low-magnification and (**b**) high-magnification fractographs of creep tested samples at 800 °C/80 MPa

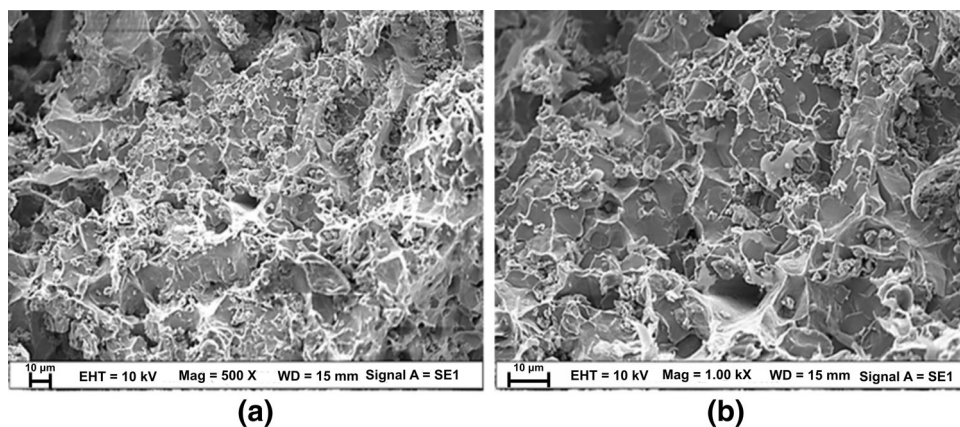(a)   (b)

Fig. 13 (**a**) Low-magnification and (**b**) high-magnification fractographs of creep tested samples at 900 °C/47 MPa

(a)   (b)

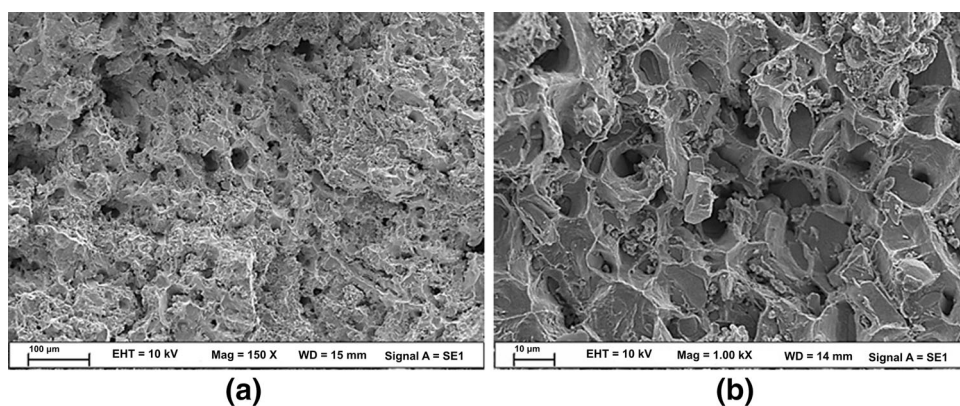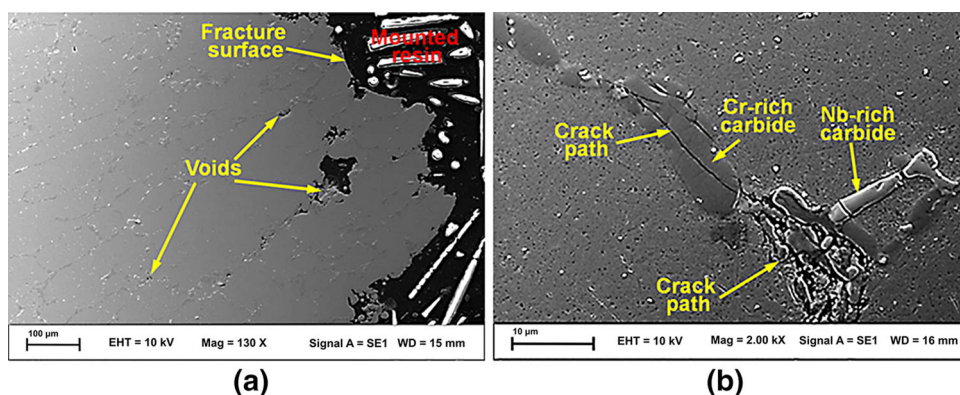**Fig. 14** SEM images at (**a**) low magnification and (**b**) higher magnification of cracks along the longitudinal section after fracture at 850 °C/68 MPa

(a)   (b)

micro-alloyed steel is in the range of +5 to −7%. The root mean square (RMS) error in the prediction of minimum creep rate is determined to be 3.75×10^{-5} s^{-1}. The statistical analysis establishes the confidence in the constitutive model for prediction of minimum creep rate at various combinations of stress and temperature within the test condition for the micro-alloyed steel.

Figure 12(a) and (b) shows the SEM micrographs of the fractured surface of the creep tested specimen at 800 °C/ 80 MPa. Micrograph obtained at low magnification (Fig. 12a) reveals quasi-cleavage features. High-magnification micrograph (Fig. 12b) reveals cleavage features

along with micro-cracks at the particle matrix interface regions. At some regions, dimple features are also observed. Similar observation is also observed in tensile specimen tested at 800 °C. Fractographs of specimen tested at 900 °C/47 MPa shown in Fig. 13(a) and (b) reveal the failure of the sample in fully ductile manner. Almost the entire surface shows dimple feature characteristics of micro-void nucleation and coalescence.

Figure 14(a) and (b) shows the SEM micrographs of the longitudinally sectioned specimen creep tested at 850 °C/ 68 MPa. Low-magnification micrograph (Fig. 14a) reveals the presence of voids at grain boundary regions near the

fractured surface. Observation under high magnification (Fig. 14b) reveals the particle fracture and presence of voids at the carbide–matrix interface regions. The creep strain of 0.28 and the total strain to failure during the tensile testing above 800 °C indicate that the failure is by a ductile mode of failure. From the fracture features, it can be ascertained that the creep failure process is by nucleation of voids at the particle–matrix interface and/or particle fracture, growth of these voids along the grain boundaries and final coalescence.

Conclusions

The creep deformation behavior of HP40Nb micro-alloyed steel were investigated by constant stress creep tests performed at temperatures 800, 850, and 900 °C and stresses of 47–80 MPa. Carbide network of Cr-rich Cr_7C_3 and $Cr_{23}C_6$, Nb-rich NbC, and (Nb-Ti)-rich were observed in the austenite matrix. The Young's modulus, yield strength and ultimate tensile strength of the micro-alloyed steel decreased with the increase in temperature due to coarsening of second-phase particles. The activation energy for creep deformation in the stress and temperature ranges studied indicated higher Q value than Q_c due to obstacle of second-phase particles during dislocation motion. The constants, A and n, in the power-law constitutive equation for the prediction of minimum creep rate were determined for the micro-alloyed steel. The stress exponent along with corresponding activation energy of the micro-alloyed steel revealed that dislocation creep was the dominant creep mechanism. The movement of dislocations involved the diffusion of vacancies or interstitials. The power-law constitutive equation could predict the minimum creep rate in the stress and temperature ranges studied with a coefficient of determination 0.995 and RMS error of 3.75 × 10^{-5} s^{-1}. The percentage deviation between experimental values and predicted values were in the range of +5 and −7%. Fracture surfaces above 800 °C exhibited predominately ductile fracture. The creep failure of the material is by a process of crack nucleation and growth through the grain boundaries.

References

1. A. Alvino, D. Ramires, A. Tonti, D. Lega, Influence of chemical composition on microstructure and phase evolution of two HP heat resistant stainless steels after long term plant-service aging. Mater. High Temp. **31**(1), 2–11 (2014)

2. Z. Liu, P. La, L. Zeng, W. Wang, H. Xue, Y. Hao, Effect of aluminum on microstructure of HP40 steel. *Proceedings of Sino-Swedish Structural Materials Symposium* (2007), pp. 373–377

3. J. Yan, Y. Gao, F. Yang, C. Yao, Z. Ye, D. Yi, S. Ma, Effect of tungsten on the microstructure evolution and mechanical properties of yttrium modified HP40Nb alloy. Mater. Sci. Eng. A **529**, 361–369 (2011)

4. W.Z. Wang, F.Z. Xuan, Z.D. Wang, B. Wang, C.J. Liu, Effect of overheating temperature on the microstructure and creep behavior of HP40Nb alloy. Mater. Des. **32**(7), 4010–4016 (2011)

5. K. Guan, Q. Wang, Analysis of failed electron beam welds in ethylene cracking tubes. Eng. Fail. Anal. **18**, 1366–1374 (2011)

6. A.K. Ray, S.K. Sinha, Y.N. Tiwari, J. Swaminathan, G.D.S. Chaudhuri, R. Singh, Analysis of failed reformer tubes. Eng. Fail. Anal. **10**, 351–362 (2003)

7. A. Alvino, D. Lega, F. Giacobbe, V. Mazzocchi, A. Rinaldi, Damage characterization in two reformer heater tubes after nearly 10 years of service at different operative and maintenance conditions. Eng. Fail. Anal. **17**, 1526–1541 (2010)

8. S.A.J. Jahromi, M.N. Khani, Creep life assessment of primary reformer HP40-Nb modified steel tube of an ammonia plant. IJE Trans. B Appl. **17**, 183–190 (2004)

9. A. Ghatak, P.S. Robi, Creep behavior and creep life assessment of HP40Nb reformer steel. Int. J. Res. Eng. Appl. Sci. **5**, 98–105 (2015)

10. J. Swaminathan, K. Guguloth, M. Gunjan, P. Roy, R. Ghosh, Failure analysis and remaining life assessment of service exposed primary reformer heater tubes. Eng. Fail. Anal. **15**(4), 311–331 (2008)

11. C.R. Barrett, A.J. Ardell, O.D. Sherby, Influence of modulus on the temperature dependence of the activation energy for creep at high temperatures. Trans. TMS-AIME **230**, 200–205 (1964)

12. J.E. Dorn, *Energetics in Metallurgical Phenomena* (Gordon and Breach, New York, 1965)

13. M. Malu, J.K. Tien, The elastic modulus correction term in creep activation energies: applied to oxide dispersion strengthened superalloy. Scr. Metall. Matter. **9**(10), 1117–1120 (1975)

14. L.H. De Almeida, A.F. Ribeiro, I.L. May, Microstructural characterization of modified 25Cr-35Ni centrifugally cast steel furnace tubes. Mater. Charact. **49**, 219–229 (2002)

15. A.K. Ray, S. Kumar, G. Krishna, M. Gunjan, B. Goswami, S.C. Bose, Microstructural studies and remnant life assessment of eleven years service exposed reformer tube. Mater. Sci. Eng. A **529**, 102–112 (2011)

16. S. Latha, M.D. Mathew, P. Parameswaran, K.B.S. Rao, S.L. Mannan, Thermal creep properties of alloy D9 stainless steel and 316 stainless steel fuel clad tubes. Int. J Press. Vessels Pip. **85**, 866–870 (2008)

17. D.B. Park, S.M. Hong, K.H. Lee, M.Y. Huh, J.Y. Suh, S.C. Lee, W.S. Jung, High-temperature creep behavior and microstructural evolution of an 18Cr9Ni3CuNbVN austenitic stainless steel. Mater. Charact. **93**, 52–61 (2014)

18. M.D. Mathew, G. Sasikala, K.B.S. Rao, S.L. Mannan, Influence of carbon and nitrogen on the creep properties of type 316 stainless steel at 873 K. Mater. Sci. Eng. A **148**, 253–260 (1991)

19. G. Pilloni, E. Quadrini, S. Spigarelli, Interpretation of the role of forest dislocations and precipitates in high-temperature creep in aNb-stabilised austenitic stainless steel. Mater. Sci. Eng. A **279**, 52–60 (2000)

20. Y. Han, M.C. Chaturvedi, A study of back stress during creep deformation of a superalloy Inconel 718. Mater. Sci. Eng. **85**, 59–65 (1987)

21. Y. Yamane, T. Takahashi, K. Nakagawa, Effect of carbide precipitates on high temperature creep of a 20Cr-25Ni austenitic stainless steel. J. Mater. Sci. Lett. **3**, 557–559 (1984)

22. D.V.V. Satyanaryana, G. Malakondaiah, D.S. Sarma, Steady state creep behavior of NiAl hardened austenitic steel. Mater. Sci. Eng. A **323**, 119–128 (2002)